

Article

The Effect of Co-Crystallising Sulphides and Precipitation Mechanisms on Sphalerite Geochemistry: A Case Study from the Hilton Zn-Pb (Ag) Deposit, Australia

Bradley Cave ^{1,*} , Richard Lilly ¹ and Wei Hong ^{1,2}

¹ Mawson Centre for Geoscience, Department of Earth Sciences, The University of Adelaide, Adelaide 5005, SA, Australia; richard.lilly@adelaide.edu.au (R.L.); wei.hong@adelaide.edu.au (W.H.)

² Mineral Exploration Cooperative Research Centre (MinEx CRC), Adelaide, SA 5005, Australia

* Correspondence: bradley.cave@adelaide.edu.au

Received: 3 August 2020; Accepted: 7 September 2020; Published: 9 September 2020



Abstract: High-tech metals including Ge, Ga and In are often sourced as by-products from a range of ore minerals, including sphalerite from Zn-Pb deposits. The Hilton Zn-Pb (Ag) deposit in the Mount Isa Inlier, Queensland, contains six textural varieties of sphalerite that have formed through a diverse range of processes with variable co-crystallising sulphides. This textural complexity provides a unique opportunity to examine the effects of co-crystallising sulphides and chemical remobilisation on the trace element geochemistry of sphalerite. Early sphalerite (sph-1) is stratabound and coeval with pyrrhotite, pyrite and galena. Disseminated sphalerite (sph-2) occurs as isolated fine-grained laths rarely associated with co-crystallising sulphides and represents an alteration selvage accompanying the precipitation of early stratabound sphalerite (sph-1). Sphalerite (sph-3) occurs in early ferroan-dolomite veins and formed from the chemical remobilisation of stratabound sphalerite (sph-1) during brittle fracturing and interstitial fluid flow. This generation of veins terminate at the interface, and occurs within clasts of the paragenetically later sphalerite-dominated breccias (sph-4). Regions of high-grade Cu (>2%) mineralisation contain a late generation of sphalerite (sph-5), which formed from the recrystallisation of breccia-type sphalerite (sph-4) during the infiltration of a paragenetically late Cu- and Pb-rich fluid. Late ferroan-dolomite veins crosscut all previous stages of mineralisation and also contain chemically remobilised sphalerite (sph-6). Major and trace elements including Fe, Co, In, Sn, Sb, Ag and Tl are depleted in sphalerite associated with abundant co-crystallised neighbouring sulphides (e.g., pyrite, pyrrhotite, galena and chalcopyrite) relative to sphalerite associated with minor to no co-crystallising sulphides. This depletion is attributed to the incorporation of the trace elements into the competing sulphide minerals. Chemically remobilised sphalerite is enriched in Zn, Cd, Ge, Ga and Sn, and depleted in Fe, Tl, Co, Bi and occasionally Ag, Sb and Mn relative to the primary minerals. This is attributed to the higher mobility of Zn, Ge, Ga and Sn relative to Fe and Co during the chemical remobilisation process, coupled with the effect of co-crystallising with galena and ferroan-dolomite. Results from this study indicate that the consideration of co-crystallising sulphides and post-depositional processes are important in understanding the trace element composition of sphalerite on both a microscopic and deposit-scale, and has implications for a range of Zn-Pb deposits worldwide.

Keywords: sphalerite; trace elements; Hilton Zn-Pb (Ag); sulphides; Mount Isa; critical metals

1. Introduction

The growth in technical innovation and an increasing drive for 'green' technology has prompted a growth in the demand for a previously underutilised set of metals and non-metals [1]. The elements Ge, Ga, In, Co and Cd are used in the production of a wide variety of technologies such as solar panels, LCD glasses, batteries, transistors and optical fibres [2]. These elements are often concentrated in polymetallic sulphide deposits, preferentially residing in sphalerite [3–5]. In order to understand the mechanisms responsible for the concentration of trace elements in sphalerite, an increasing amount of research has been dedicated to assessing the geochemistry of sphalerite from a range of Zn-deposits worldwide (e.g., [6–9]).

Previous studies have indicated that the concentrations of Mn, Fe, Ge, Ga and In are proportional to the precipitation temperature of sphalerite [8]. Ge can be upgraded in deposits by the dynamic recrystallisation of sphalerite during metamorphism [10] and high-In sphalerite can be produced by the infiltration of late Cu-bearing fluids [6]. It has also been shown that sphalerite from high-temperature magmatic fluids are enriched in In, while sphalerite derived from low-temperature crustal fluids are relatively enriched in Ga and Ge [11]. George et al. [5] showed the factors governing the partitioning trends of trace elements between sphalerite, chalcopyrite and galena included: (1) the redox state of the elements; (2) the trace element budget for each mineral and; (3) the ionic radius of the substituting element. Multiple textural varieties of sphalerite, or individual generations of sphalerite within a single ore deposit has been the focus of multiple studies [12,13], and show that trace element contents can differ substantially. Despite the continued research, two key aspects that greatly affect the trace element content of sphalerite require further investigation: (1) the effect of co-crystallising sulphides and; (2) the effect of chemical remobilisation.

The Hilton Zn-Pb (Ag) deposit, northern Australia (Figure 1) contains numerous textural varieties of sphalerite that have precipitated via different formation mechanisms and alongside a range of co-crystallising sulphides [14,15]. This study uses detailed petrography to determine the multiple stages of sphalerite and co-genetic minerals present within the deposit. This is accompanied by the trace element analysis of each sphalerite variety to determine the relationship between the trace element composition of sphalerite, the presence/absence of co-crystallising sulphides and the effect of small-scale chemical remobilisation. Understanding and interpreting the cause of variations in the trace element geochemistry of sphalerite can have potential applications to a variety of Zn-Pb deposits worldwide.

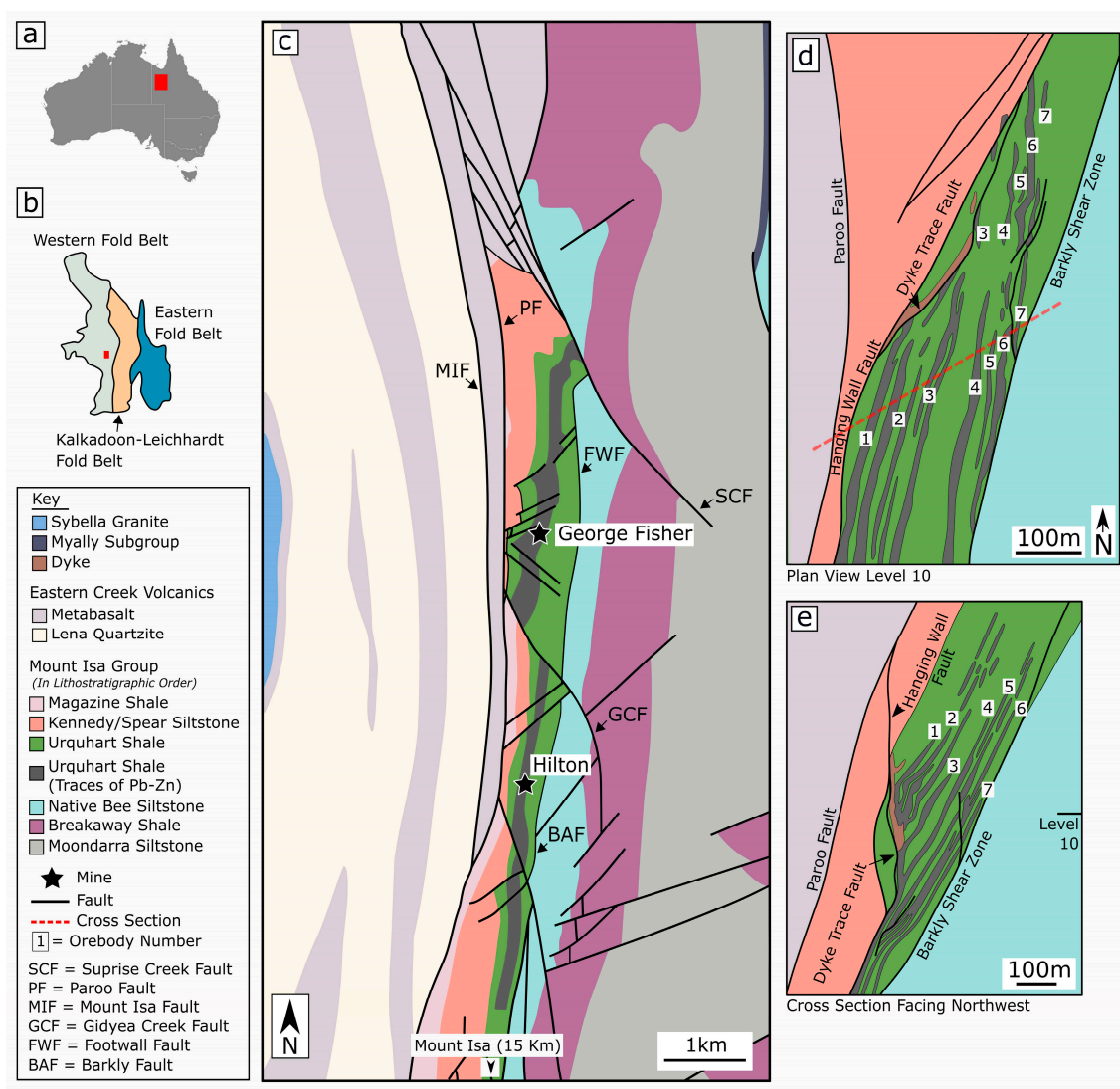


Figure 1. Location of the study area with reference to (a) Australia and (b) the Mount Isa Inlier. (c) A simplified geological map of the study area after Valenta [16] with the location of the Hilton and George Fisher Zn-Pb (Ag) deposits. (d) Plan view of the Hilton Zn-Pb (Ag) deposit showing the seven north to south trending stratabound ore zones. (e) A schematic cross-section of the Hilton Zn-Pb (Ag) deposit facing northwest. Figure 1d,e have been updated from Valenta [17] using available mine models.

2. Background

2.1. Regional Geology

The late Paleoproterozoic to early Mesoproterozoic McArthur Basin and the Mount Isa Inlier in northern Australia are host to numerous Zn-Pb deposits that comprise the Carpentaria—Mount Isa Zinc Belt [18]. The Hilton Zn-Pb (Ag) deposit is the focus of this study. This deposit is located in the Western Fold Belt of the Paleoproterozoic Mount Isa Inlier, approximately 20 km north of the Mount Isa Cu-Zn-Pb (Ag) deposit (Figure 1a–c). The Western Fold Belt hosts three major Superbasins; (1) Leichhardt Superbasin (1800–1750 Ma); (2) Calvert Superbasin (1750–1690 Ma); and (3) Isa Superbasin (1690–1575 Ma) [19]. The Isa Superbasin is further divided into the Gun, Loretta, River, Term, Lawn, Wilde and Doom supersequences, which are composed of various turbidites, stromatolitic dolostones and carbonaceous shales that were deposited in a shallow to deep marine environment [19,20]. The Gun

and Loretta supersequences contain the regionally extensive Mount Isa Group (Figure 1c) and are dominated by deep water turbiditic rhythmites [21]. Basin development was terminated by the onset of the 1610–1500 Ma Isan Orogeny [19,22–24].

The Mount Isa region has undergone four major deformation events (D_1 – D_4) during the Isan Orogeny. D_1 deformation consisted of N–S directed compression that produced a bedding-parallel foliation in carbonaceous and phyllosilicate units in the Hilton area [14,25]. D_2 deformation is characterised by E–W shortening that produced district-scale upright folds with N–S trending axes [25,26]. Early studies dated this deformation event at ca 1555–1530 Ma [25,27]. However, more recent geochronology studies favour D_2 deformation at 1575 Ma [28,29]. D_2 deformation was coeval with regional peak metamorphism, locally constrained to temperatures of ~200 °C by bitumen reflectance data [30] at the nearby George Fisher Zn–Pb (Ag) deposit (Figure 1c). D_3 deformation (formally $D_{2.5}$ by Bell and Hickey [31]) is only present in localised regions throughout the Mount Isa Inlier, and produced highly asymmetric deflections in S_2 fabric and bedding with top to the east vergence [31]. D_4 deformation produced NNW–SSE trending inclined to recumbent folding with amplitudes of cm to 10's of meters at the Hilton deposit [14]. Post to late- D_4 faults offset Pb–Zn orebodies at Hilton from 2–100 m [14].

2.2. Hilton Zn–Pb (Ag) Deposit Geology

Economic Zn–Pb mineralisation is hosted by the ca. 1650 Ma Urquhart Shale and occurs as seven (1–7) stratabound orebodies (Figure 1d,e). The genesis of the Hilton Zn–Pb (Ag) deposit is controversial, with both syn-sedimentary [14] and syn-deformational carbonate replacement [32] models proposed. The north of the orebody is bounded by the Dyke Trace Fault Zone, the east by the Barkly Shear Zone, the west by the Hanging Wall Fault and the south by an unnamed northwest-southeast striking sinistral fault (Figure 1d,e; [17]). The orebodies are divided into the hanging wall orebodies (1–3) and the footwall orebodies (4–7), which are separated by an un-mineralised siltstone pillar. The highest Zn and Pb values occur near the Dyke Trace Fault in the hanging wall orebodies and laterally up-dip [15]. Pb grades shows a northerly trend associated with the hanging wall fault zone, with high-grade Pb (>8%) primarily constrained to the lower 2 and 3 orebodies [15]. Mineralisation is constrained to stratabound regions that have undergone multiple stages of pre-mineralisation alteration, and occur as bedding-parallel veins and various polymetallic sphalerite- and galena-dominant breccias. A chalcopyrite and pyrrhotite-rich zone occurs adjacent to the Hanging Wall Fault within an area associated with syn- to post- D_2 movement [17]. Elevated Cu (>1%) is restricted to the 1–3 orebodies, and shows a strong spatial relationship to the major north-south sub-vertical shear/dyke system [15,17]. High-grade Cu (>2%) appears in Pb- and Zn-bearing breccias, and has a close spatial relationship with high-grade Pb (>8%) [15].

3. Methods

3.1. Sampling Selection

Five sections of drill core that intersect multiple orebodies on level 5, 12 and 14 were logged in detail and sampled. Samples were selected on the basis of mineralisation styles and temporal relationships. This resulted in a diverse sample suite of 21 sphalerite-bearing samples. The samples were made into polished resin blocks and polished thin sections following standard procedures. The polished resin blocks were used for subsequent LA-ICP-MS analysis.

3.2. LA-ICP-MS Analyses

3.2.1. Spot Analyses

LA-ICP-MS spot analyses of sphalerite were carried out at Adelaide Microscopy using a NWR213 (Omaha, NE, USA) solid state 213 nm laser ablation system coupled with an Agilent 7900 (Santa Clara,

CA, USA) quadrupole ICP-MS. Ablation was conducted in an atmosphere of He (0.6 L/min) that was mixed with Ar (0.88 L/min) upon leaving the ablation cell. The material then passes through a pulse-homogenisation device before being introduced to the ICP torch. Ablation spot size ranged from 10–70 μm . The repetition rate of the laser was 5 Hz with a consistent fluence of $\sim 4 \text{ J/cm}^2$. Pre-ablation consisted of 5 pulses, followed by a 20 s delay to allow adequate cell wash out before the proceeding analyses. Data collection consisted of 30 s background collection, followed by 40 s of ablation. The Isotopes monitored include: ^{27}Al , ^{34}S , ^{29}Si , ^{55}Mn , ^{57}Fe , ^{59}Co , ^{60}Ni , ^{65}Cu , ^{66}Zn , ^{69}Ga , ^{71}Ga , ^{72}Ge , ^{73}Ge , ^{75}As , ^{77}Se , ^{95}Mo , ^{109}Ag , ^{111}Cd , ^{113}In , ^{115}In , ^{118}Sn , ^{121}Sb , ^{125}Te , ^{182}W , ^{197}Au , ^{201}Hg , ^{205}Tl , ^{206}Pb , ^{207}Pb , ^{208}Pb , and ^{209}Bi . The dwell time of each isotope was 0.02 s, except for ^{27}Al , ^{29}Si , ^{34}S , and ^{55}Mn with dwell times of 0.005 s and ^{59}Co , ^{60}Ni , ^{65}Cu , ^{66}Zn , ^{206}Pb , ^{207}Pb , and ^{208}Pb with dwell times of 0.01 s. The GSD-1G (USGS) and STDGL3 (CODES, University of Tasmania; [33]) standards were analysed using a 70 μm diameter spot size with a 25:2 standard sample bracketing approach.

3.2.2. Trace Element Maps

LA-ICP-MS trace element maps were produced using a spot size of 16 μm with a scan speed of 16 $\mu\text{m/s}$. The isotopes: ^{27}Al , ^{34}S , ^{29}Si , ^{55}Mn , ^{57}Fe , ^{59}Co , ^{60}Ni , ^{65}Cu , ^{66}Zn , ^{69}Ga , ^{71}Ga , ^{72}Ge , ^{73}Ge , ^{77}Se , ^{109}Ag , ^{111}Cd , ^{115}In , ^{118}Sn , ^{121}Sb , ^{125}Te , ^{205}Tl , ^{208}Pb and ^{209}Bi were analysed. A dwell time of 0.002 s was used for isotopes ^{27}Al , ^{29}Si and ^{34}S , 0.005 s for isotopes ^{55}Mn and ^{57}Fe , and a dwell time of 0.01 s was used for the collection of the remaining isotopes. The repetition rate used was 10 Hz with a fluence of $\sim 4 \text{ J/cm}^2$. Pre-ablation consisted of a single transect across the same path used for analysis, followed by a 20 s delay to allow adequate cell wash out. The scan time for each line was 153.875 and 138.369 s for maps that are located between sph-4 and sph-5, and sph-4 and sph-6 respectively, which followed a 10 s background collection. The GSD-1G (USGS) and STDGL3 (CODES, University of Tasmania; [33]) standards were analysed every 20 transects using a 70 μm spot size.

3.2.3. Data Processing

LA-ICP-MS spot analyses were processed using LADR (Moonah, TAS, Australia) data reduction software [34]. Each analysis was checked for mineral inclusions by inspecting the time-resolved profile of each individual isotope. Data compromised by obvious inclusions, as inferred by large irregular spikes in any element, were rejected, and inclusion-free portions of the time-resolved profile was selected. The STDGL3 standard was used as the primary standard to correct for instrument drift and mass bias, with GSD-1G used as a secondary standard. For the elements Al, Si and Ga, GSD-1G was used as the primary standard. ^{113}In and ^{115}In were corrected for isobaric interferences from ^{111}Cd and ^{118}Sn respectively by using the measured ^{111}Cd and ^{118}Sn isotopes and assuming normal isotopic abundances. To account for solid-solution between Zn, Fe and Cd in the analysed sphalerite, the isotopes listed in Section 3.2.1. (excluding: ^{29}Si , ^{27}Al , ^{71}Ga , ^{73}Ge , ^{113}In , ^{206}Pb and ^{207}Pb) were normalised to a total of 100 wt% assuming mono-sulphide stoichiometry. Where multiple isotopes were measured, the concentration of the isotopes ^{115}In , ^{208}Pb , ^{69}Ga and ^{72}Ge were preferentially used. To check the validity of this method, the concentration of Zn, Fe and Cd was measured on multiple samples using a Cameca SXFive (Fitchburg, MA, USA) Electron Microprobe at Adelaide Microscopy (Supplementary Materials Table S1). A comparison between the normalised LA-ICP-MS data and the microprobe show good agreement, and are always within analytical error of each instrument.

LA-ICP-MS trace element maps were produced using Iolite [35]. Instrumental drift was corrected through the Baseline_Subtract data reduction scheme [36]. As the major chemistry of each sphalerite variety differs considerably, counts per second (cps) maps were produced. This allows for a direct comparison between the relative abundance of trace-elements in each variety of sphalerite, as well as all other co-crystallising minerals.

4. Sphalerite Textures and Generations

The paragenesis documented from the samples collected at Hilton (Figure 2) is similar to the paragenesis recognised by Chapman [37] and Rieger et al. [38] at the nearby George Fisher Zn-Pb (Ag) deposit. Broadly, early stratabound Zn mineralisation is followed by breccia-style Zn-Pb mineralisation with intermittent stages of ferroan-dolomite veining (Figure 2). Each sphalerite stage is documented in detail below.

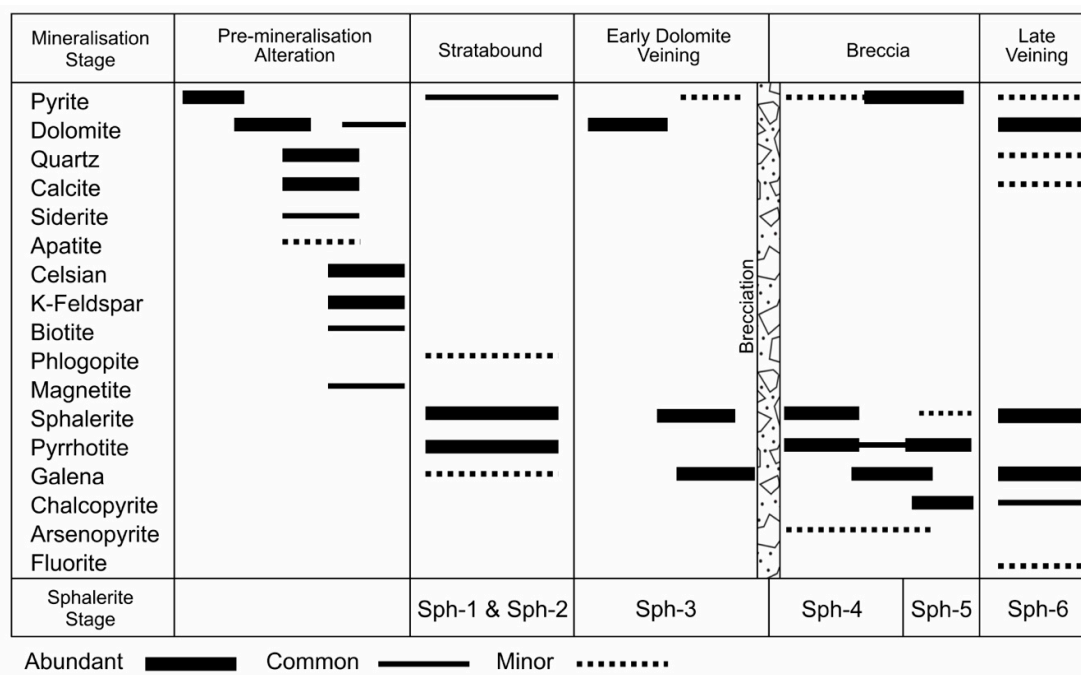


Figure 2. Paragenesis of the Hilton Zn-Pb (Ag) deposit based on the samples from this study. Pre-mineralisation alteration is followed by stratabound mineralisation containing sph-1 and sph-2. Early dolomite veins contain sph-3 and are followed by a stage of brecciation and the emplacement of sph-4. This is overprinted by Pb and Cu mineralisation where sph-4 is recrystallised to produce sph-5. Multiple varieties of late veins crosscut all types of mineralisation and contain sph-6.

4.1. Stratabound Sphalerite (Sph-1)

Stratabound sphalerite (sph-1) constitutes the first major Zn mineralisation event, accounting for 6–38% of the total Zn in the drill core used in this study. Sph-1 is paragenetically early and broadly constrained to regions affected by pre-mineralisation dolomite + quartz + calcite + siderite ± apatite (Figure 3a), and often K-feldspar + celsian + biotite ± magnetite alteration. The abundance of sphalerite in this stage varies from a major (>90%) component of the mineralogy to inter-connected sphalerite grains that make up a minor (<10%) component (Figure 3a–d). Co-crystallising pyrrhotite varies from a minor (<20%) to major (>60%) component (Figure 3b,c). Fine-grained (<50 μm) galena, phlogopite and euhedral pyrite form a minor component of this stage (Figure 3d,e). Sph-1 and coeval sulphides envelope and partially replace minerals that comprise the various stages of pre-mineralisation alteration. Individual mineralised horizons vary from <1 to >20 cm in width. Sph-1 is stratabound over a deposit scale, but commonly envelopes and partially replaces discordant pre-mineralisation dolomite + quartz + calcite + siderite veins (Figure 4a).

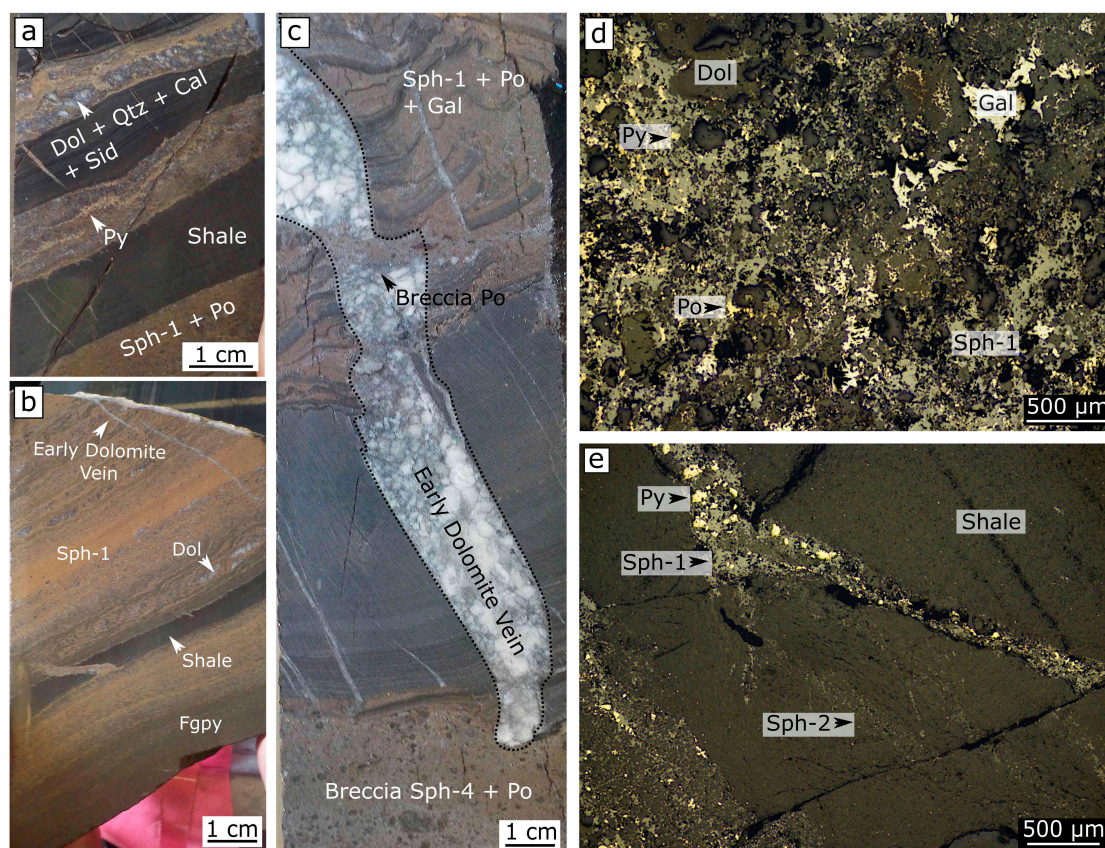


Figure 3. Sphalerite paragenesis at the Hilton Zn-Pb (Ag) deposit. (a) Sph-1 replacing a stratabound pre-mineralisation dolomite + quartz + calcite + siderite vein. (b) Sph-1 dominated stratabound mineralisation that is crosscut by an early ferroan dolomite vein. (c) Stratabound Zn mineralisation crosscut by an early dolomite vein. The early dolomite vein terminates at the interface of a Zn-dominated breccia. (d) Reflected light photomicrograph showing sph-1 with co-crystallising pyrite, pyrrhotite and galena. (e) Reflected light photomicrograph showing fine-grained disseminated sph-2 splaying from a sph-1 vein. Abbreviations: qtz = quartz, cal = calcite, sid = siderite, sph = sphalerite, dol = dolomite, fgpy = fine-grained pyrite, py = pyrite, gal = galena, po = pyrrhotite.

4.2. Disseminated Sphalerite Alteration (Sph-2)

Disseminated sphalerite (sph-2) occurs as fine to medium grains (<50 μm) that form stratabound layers that are often <1 cm in width (Figure 4a,b). On a deposit scale, disseminated sphalerite is volumetrically insignificant and does not constitute economic Zn mineralisation. Sph-2 occurs in carbonaceous shale that has been variably affected by pre-mineralisation dolomite + quartz + calcite + siderite \pm apatite and K-feldspar + celsian + biotite veining/alteration. Co-crystallising sulphides are rare in this stage, with only very minor pyrite and galena documented in the samples from this study. Disseminated sphalerite often splays from pre-mineralisation dolomitic veins (Figures 3e and 4a) and graphitic seams containing sph-1. Consistent with the interpretation of this variety of sphalerite at George Fisher by Chapman [37], sph-2 is interpreted to represent an alteration selvage associated with the emplacement of sph-1.

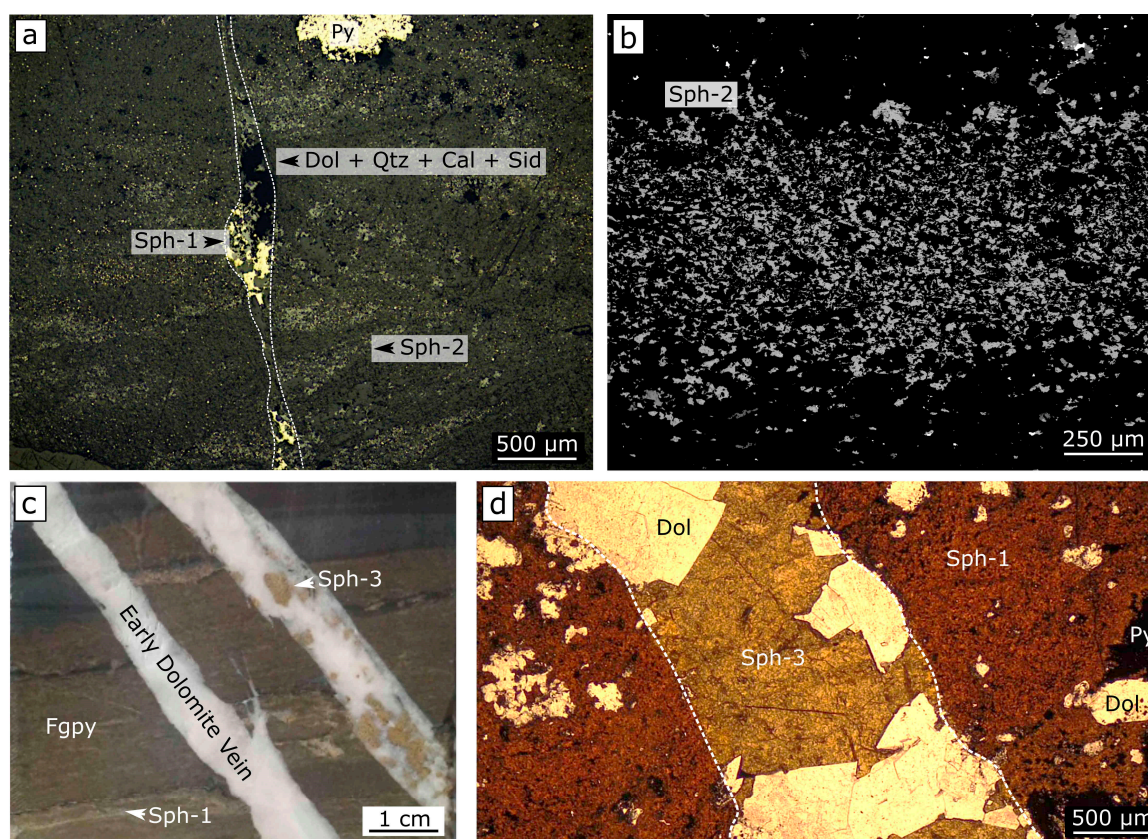


Figure 4. Sphalerite paragenesis at the Hilton Zn-Pb (Ag) deposit (continued). (a) Reflected light photomicrograph showing fine-grained disseminated sph-2 splaying out from a discordant sph-1 bearing vein. (b) Back-scattered electron image of fine-grained disseminated sph-2. (c) An early dolomite vein containing sph-3 cross-cutting a sample containing abundant fine-grained pyrite with minor sph-1. (d) Plane polarised light photomicrograph of an early dolomite vein cross-cutting stratabound sph-1 mineralisation. Note the colour difference between sph-1 and sph-3. Abbreviations: sph = sphalerite, dol = dolomite, fgpy = fine-grained pyrite, py = pyrite, qtz = quartz, cal = calcite, sid = siderite.

4.3. Sphalerite in Early Ferroan-Dolomite Veins (Sph-3)

Discordant ferroan-dolomite veins occur throughout the deposit and crosscut early sph-1 and disseminated sph-2 (Figure 3b,c and Figure 4c,d). Ferroan-dolomite veins range from 0.1–10 cm in width. Ferroan-dolomite is typically coarse-grained and highly zoned. Sph-3 and galena are present as medium- to coarse-grained components in these veins (Figure 4c,d), with fine-grained sphalerite occurring along the vein boundaries. Sph-3 is a lighter colour in plane polarised light relative to sph-1 (Figure 4d). Pyrite is rare in these veins and only occurs as isolated grains (<50 µm) along the grain boundaries of coarse-grained ferroan-dolomite. Minor veins of this stage contain abundant chlorite, which splays out from the veins and preferentially replace pre-mineralisation magnetite. Sph-3 and the co-crystallising galena in these veins are interpreted to have formed from the chemical remobilisation of sph-1, with an insignificant contribution from sph-2 during initial fracturing and subsequent interstitial fluid flow.

4.4. Sphalerite Dominated Breccias (Sph-4)

Matrix-supported breccia mineralisation constitutes the second major Zn mineralising event and is associated with the highest grades of Zn at Hilton, accounting for 62–94% of Zn in the drill core used in this study. Shale clasts within the breccia contain fine-grained pyrite, dolomite + quartz + calcite +

siderite ± apatite veins, K-feldspar + celsian + magnetite alteration, sph-1 and sph-2 mineralisation, and early ferroan-dolomite veins (Figure 5a,b). Core samples clearly outline the relationship between stratabound mineralisation, early ferroan-dolomite veins and breccia mineralisation. Figure 3c shows that stratabound sph-1 is crosscut by early ferroan-dolomite veins, which terminate at the interface of sph-4 bearing breccia mineralisation. Similar to stratabound mineralisation, the co-crystallising sulphides present in sphalerite-dominated breccias are pyrite, pyrrhotite (Figure 5a–d) and arsenopyrite.

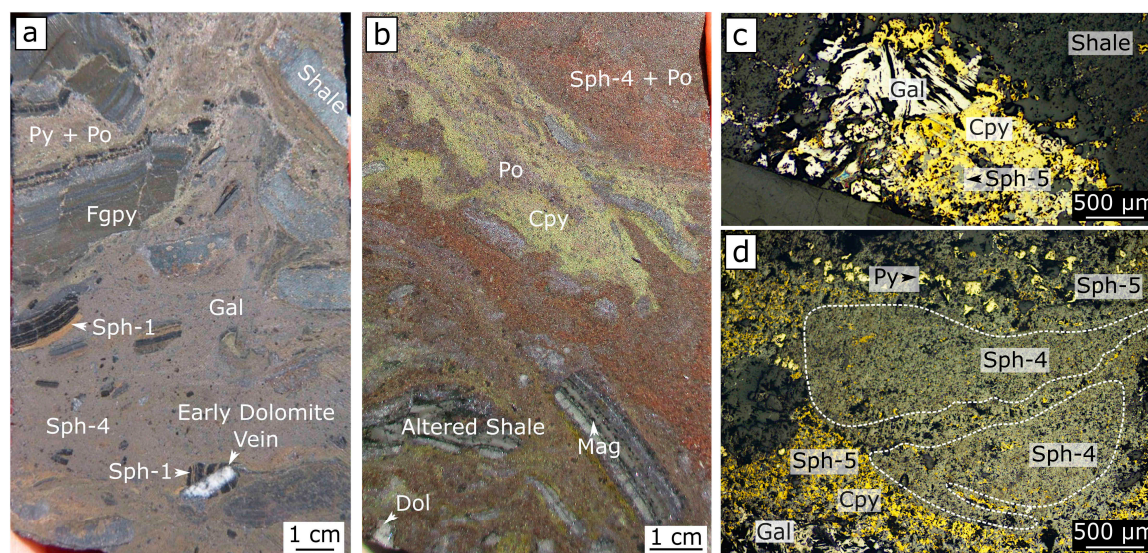


Figure 5. Sphalerite paragenesis at the Hilton Zn-Pb (Ag) deposit (continued). (a) Polymetallic sulphide-rich breccia containing sph-4, abundant pyrrhotite and high grade Pb mineralisation. Note the presence of early stratabound Zn mineralisation and early dolomite veins within the clasts of shale. (b) Polymetallic breccia containing abundant pyrrhotite and chalcopyrite that overprints sph-4. (c,d) Reflected light photomicrographs highlighting the relationship between high-grade Cu mineralisation and sph-5. Note the recrystallisation of sph-4 to form sph-5 in Figure 5d. Abbreviations: sph = sphalerite, dol = dolomite, fgpy = fine-grained pyrite, py = pyrite, gal = galena, po = pyrrhotite, cpy = chalcopyrite, mag = magnetite.

4.5. Sphalerite in Chalcopyrite Dominated Breccias (Sph-5)

Chalcopyrite-bearing breccias are the main source of Cu mineralisation at Hilton and are restricted to the 1–3 orebodies. Chalcopyrite and pyrrhotite are the dominant sulphides with variable amounts of pyrite and galena (Figure 5b–d). Chalcopyrite-dominated breccias frequently overprint and replace sph-4 dominant breccias (Figure 5b–d). Chalcopyrite and pyrrhotite often occupy texturally late sites between brecciated clasts of shale and the sphalerite-dominated breccia, are situated in veins that penetrate fragmented breccia clasts, and in discordant veins that splay out from sulphide-dominated breccias into the neighbouring shale. Core from this study records Cu values as high as 2.77%, with Cu values regularly exceeding 0.5%. In regions where Cu mineralisation has overprinted sphalerite-dominated breccias, a relatively uncommon late stage of sphalerite (sph-5) is recognised. Sph-5 penetrates sph-4 and is coeval with abundant neighbouring chalcopyrite, pyrrhotite, pyrite, galena (Figure 5d) and arsenopyrite. Sph-5 is interpreted as sph-4 that has been recrystallised during subsequent Cu mineralisation.

4.6. Sphalerite in Late Ferroan-Dolomite Veins (Sph-6)

Multiple styles of late veins crosscut all previous stages of mineralisation (Figure 6a–d). Ferroan-dolomite + calcite + quartz veins are typically crystalline and contain medium- to coarse-grained sphalerite and galena with minor chalcopyrite, pyrrhotite and pyrite. Galena is more abundant in these late veins relative to the early ferroan-dolomite veins. Other styles of

these veins include sphalerite- and galena-dominant (Figure 6c), galena-dominant with minor sphalerite, chalcopyrite and pyrite (Figure 6d) and pyrite-, chalcopyrite- and pyrrhotite-dominant veins. Late non-sulphide veins include calcite and fluorite-dominant and chlorite-dominant veins. Consistent with sph-3 situated in early ferroan-dolomite veins, sph-6 in late ferroan-dolomite veins are interpreted to have formed from the chemical remobilisation of earlier sphalerite generations upon fracturing and interstitial fluid flow. As only sph-6 that veined sph-4 breccias were analysed, we have assumed that Zn was locally derived from the sph-4 breccias.

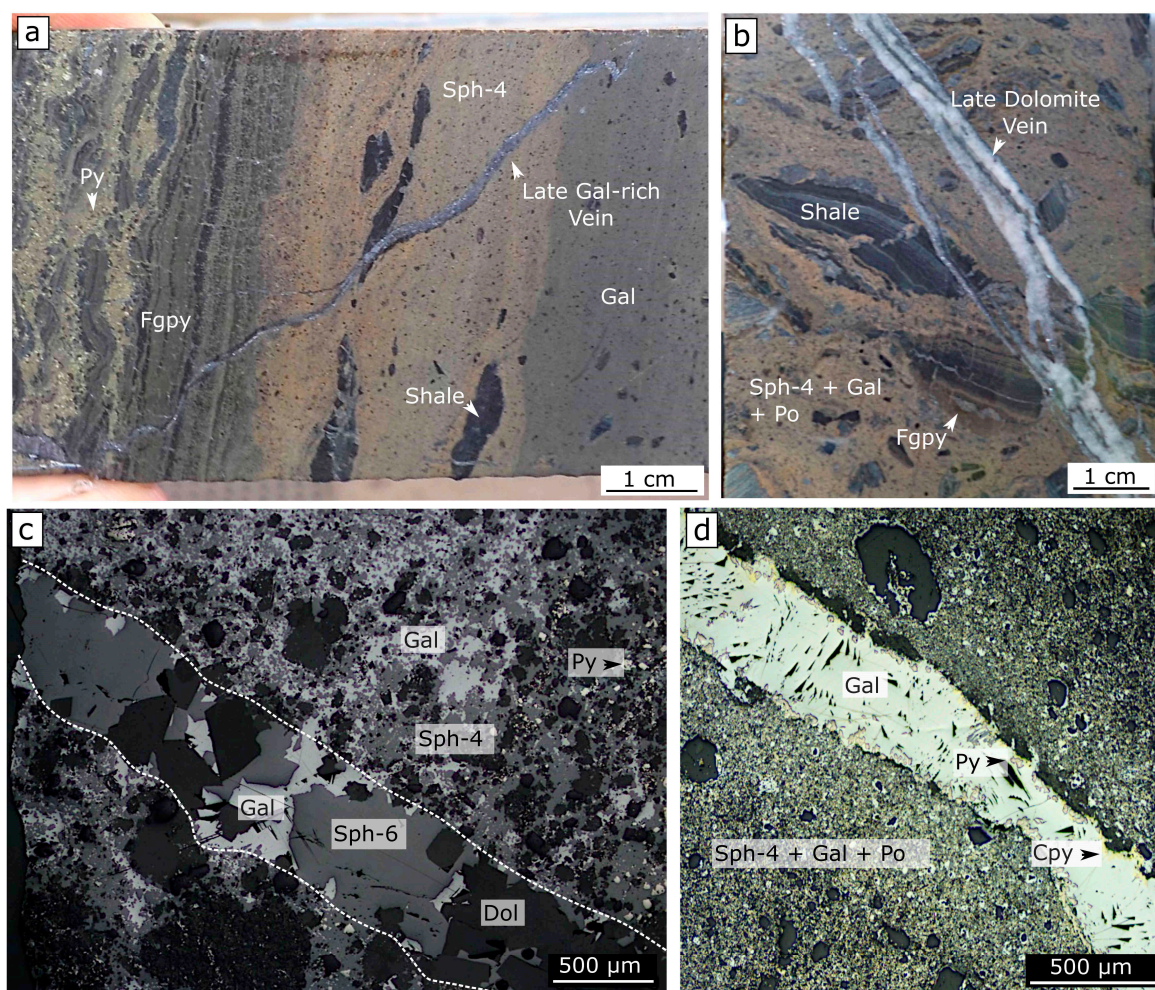


Figure 6. Sphalerite paragenesis at the Hilton Zn-Pb (Ag) deposit (continued). (a,b) Polymetallic sulphide-rich breccias cross-cut by late dolomite and sulphide-rich veins containing sph-6 and galena. (c,d) Reflected light photomicrographs of late sph-6 bearing veins cross-cutting sph-4 breccia-stage mineralisation. Abbreviations: sph = sphalerite, dol = dolomite, fgpy = fine-grained pyrite, py = pyrite, gal = galena, po = pyrrhotite, cpy = chalcopyrite.

5. Results

A total of 464 LA-ICP-MS spot analyses were conducted in this study and are reported in Supplementary Materials Table S2. This includes 109 spots on sph-1, 36 spots on sph-2, 40 spots on sph-3, 200 spots on sph-4 and 79 spots on sph-6. Due to the uncommon occurrence of sph-5, no spot analyses were acquired on this type of sphalerite. However, a trace element map was produced across a boundary between sph-4 and sph-5 to allow for a direct geochemical comparison. Sphalerite from the Hilton Zn-Pb (Ag) deposit has measurable concentrations of Mn, Co, Cu, Ga, Ge, Ag, Cd, In, Sn, Sb,

Tl, Pb and Bi (Figure 7; Supplementary Materials Table S2). The elements Mo, Se, As, Te, Ni and Au were typically below the detection limit of the ICP-MS and are therefore not used in this study.

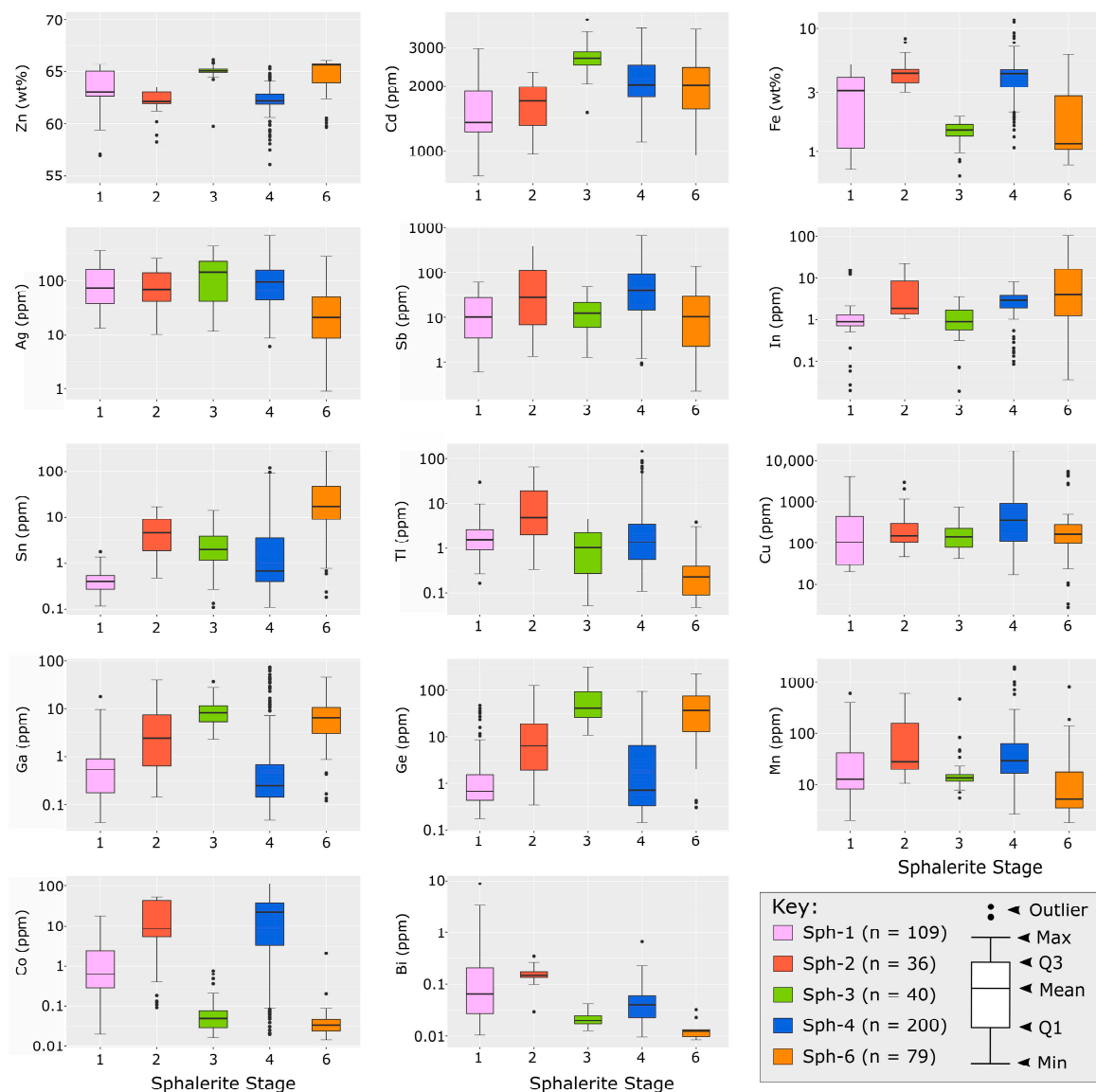


Figure 7. Box and whiskers plots of the trace elements in sphalerite analysed in this study. The box and whiskers plots are grouped into the separate sphalerite varieties.

To minimise the effect of inclusions within the sphalerite data, inclusion-free portions of the time-resolved depth profile were selected for each individual analysis. As the ablation size is significantly larger than the ablated mineral inclusions, a degree of inhomogeneity within the time-resolved depth profiles is unavoidable. The elements Zn, Fe, Cd, In and Sn consistently have smooth time-resolved depth profiles, suggesting they are homogeneously distributed over the size of the analysed spot. The elements Mn, Sb, Ag, Cu, Co, Tl, Ge and Ga show both homogeneous and heterogeneous time-resolved depth profiles, indicating their presence as both lattice-bound constituents and/or micro-scale inclusions carrying these elements. Pb and Bi always possess heterogeneous time-resolved depth profiles, indicating the presence of micron-scale inclusions of minerals carrying these elements.

5.1. LA-ICP-MS Spot Analysis

Median Fe and Zn concentrations of sph-1 are 2.73 wt% and 63.45 wt%, while sph-2 has median Fe and Zn concentrations of 4.36 wt% and 62.20 wt% (Figure 7; Table 1). Disseminated sph-2 contains higher median concentrations of Mn, Co, Ga, Ge, Cd, In, Sn, Sb and Tl than stratabound sph-1 (Figure 7; Table 1). The interquartile ranges of Co, Sn, In, Ga, Ge and Tl show minor to no overlap, indicating a significant enrichment in sph-2 relative to sph-1 (Figure 7). The concentrations of Cu and Ag do not show any considerable differences between sph-1 and sph-2.

Sph-3 in early ferroan-dolomite veins has median Fe and Zn concentrations of 1.44 wt% and 65.00 wt%, respectively (Table 1). Sph-3 has elevated concentrations of Zn, Ga, Ge, Cd and Sn, and lower concentrations of Co, Bi and Fe relative to sph-1 (Table 1; Figure 7). Ga and Ge are significantly enriched in sph-3 relative to sph-1 with median values of 9.80 ppm and 72.38 ppm, respectively (Table 1). Significant enrichments are also documented in the concentration of Cd and Sn, which do not have overlapping interquartile ranges with sph-1 (Figure 7).

Sph-6 in late cross-cutting ferroan-dolomite veins have median Fe and Zn concentrations of 2.02 wt% and 64.69 wt% while sph-4 has median concentrations of Fe and Zn of 4.15 wt% and 62.16 wt% (Table 1). Sph-6 in late cross-cutting veins has lower concentrations of Fe, Mn, Co, Ag, Sb, Tl and Bi, and higher concentrations of Zn, Ge, Ga and Sn relative to sph-4 (Table 1; Figure 7). The relative enrichments of Ga, Ge, Sn and Zn in sph-4 relative to sph-6 are consistent with the differences in the geochemistry between sph-1 and sph-3, which are interpreted to have formed from the same process. The largest depletion of trace elements in sph-6 relative to sph-4 are Tl, Bi and Co.

Table 1. The minimum, median, standard deviation and maximum values for the trace elements in sphalerite analysed in this study. All values are in ppm unless otherwise specified.

Sphalerite	Descriptives	Zn (wt%)	Cd	Fe (wt%)	Ag	Sb	In	Sn
Sph-1	Min	56.88	768	0.71	13.28	0.61	0.02	0.00
	Median	63.45	1515	2.73	104.79	16.60	2.97	0.44
	StDev	1.59	439	1.38	85.72	15.21	4.87	0.27
	Max	65.74	2968	5.09	361.09	61.96	15.53	1.75
Sph-2	Min	58.22	970	3.00	10.28	1.39	1.05	0.00
	Median	62.20	1657	4.36	91.13	73.96	5.92	5.78
	StDev	1.14	387	1.12	68.27	96.71	7.02	4.84
	Max	63.49	2306	8.29	261.32	383.10	22.50	16.78
Sph-3	Min	59.76	1501	0.63	11.77	1.32	0.00	0.11
	Median	65.00	2676	1.44	152.99	14.52	1.00	2.95
	StDev	0.93	412	0.30	116.95	10.95	0.85	2.91
	Max	66.18	4051	1.92	449.83	49.36	3.54	14.00
Sph-4	Min	54.49	1098	1.30	6.04	0.89	0.00	0.00
	Median	62.16	2132	4.15	114.50	70.67	3.00	5.52
	StDev	1.54	430	1.41	92.82	86.35	1.49	15.76
	Max	65.43	3711	11.79	692.70	673.50	8.12	119.94
Sph-6	Min	59.66	955	0.77	0.90	0.23	0.04	0.18
	Median	64.69	2025	2.02	40.67	21.08	14.21	36.55
	StDev	1.69	633	1.48	51.80	27.64	22.31	49.12
	Max	66.10	3666	6.17	283.47	140.94	103.88	272.93
Sphalerite	Descriptives	Tl	Cu	Ga	Ge	Mn	Co	Bi
Sph-1	Min	0.00	19.86	0.00	0.00	2	0.00	0.01
	Median	2.20	502.51	0.95	3.28	40	1.49	0.02
	StDev	3.13	816.98	2.07	8.53	79	2.61	0.01
	Max	29.80	4077.06	18.32	46.26	611	17.81	0.06

Table 1. Cont.

Sphalerite	Descriptives	Tl	Cu	Ga	Ge	Mn	Co	Bi
Sph-2	Min	0.00	46.87	0.00	0.00	11	0.00	0.02
	Median	13.25	378.55	5.04	14.40	105	16.22	0.10
	StDev	17.23	591.96	9.26	28.04	129	19.19	0.03
	Max	66.51	2984.88	39.53	124.77	613	53.31	0.16
Sph-3	Min	0.05	42.45	2.34	10.78	5	0.00	0.01
	Median	1.39	191.10	9.80	72.38	30	0.10	0.01
	StDev	1.23	167.01	6.95	74.80	74	0.17	0.00
	Max	4.55	751.87	36.71	314.16	478	0.76	0.02
Sph-4	Min	0.00	16.92	0.00	0.00	3	0.00	0.01
	Median	7.07	1017.44	4.18	5.62	80	21.14	0.03
	StDev	17.20	1824.00	11.98	16.03	218	23.28	0.02
	Max	146.81	17,137.82	75.14	94.39	1989	113.56	0.13
Sph-6	Min	0.00	2.77	0.12	0.30	2	0.00	0.01
	Median	0.35	549.30	8.59	56.66	25	0.04	0.01
	StDev	0.73	1253.63	8.79	60.14	93	0.23	0.01
	Max	3.78	5621.73	47.21	229.28	810	2.04	0.08

5.2. LA-ICP-MS Trace Element Maps

A set of trace element maps was produced between the interface of sph-4 and sph-5 (Figure 8). The trace element maps show that sph-5 has lower concentrations of Ga, Ge, Ag, In, Sn, Sb and Tl relative to sph-4. The elements Ga, Ge, In, Sn, Sb and Tl appear to be almost entirely depleted in sph-5. Contrastingly, sph-5 has comparably higher concentrations of Zn, Cd and Pb relative to sph-4. The elements Ge and Pb, and to some extent Ga are heterogeneously distributed in the analysed sph-4, indicating that high concentrations of these elements are associated with the presence of mineral inclusions (Figure 8). The highest concentration of Fe in the analysed section is consistent with the presence of pyrite and chalcopyrite.

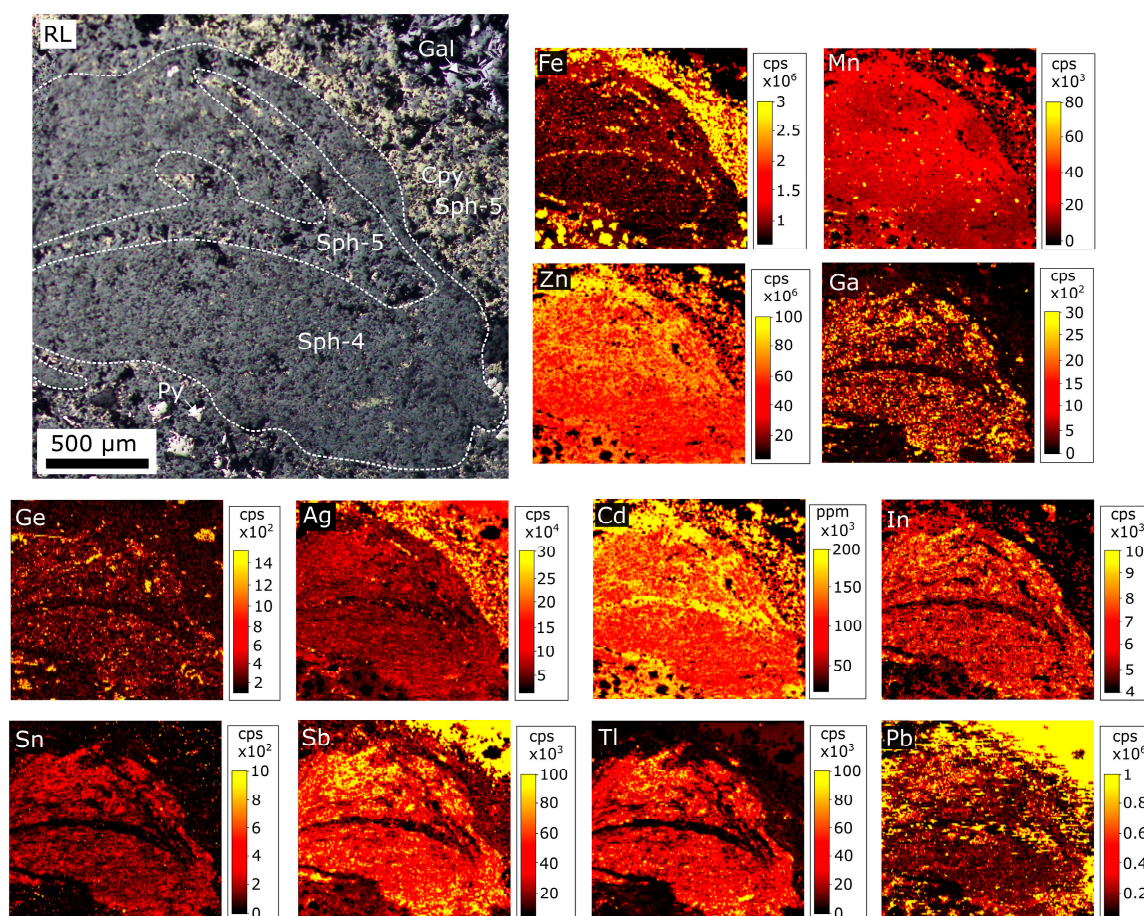


Figure 8. LA-ICP-MS trace element maps across a sample containing sph-4 and recrystallised sph-5. These maps show that sph-5 is depleted in Ge, Ga, In, Sn, Sb, Ag and Tl, and enriched in Cd and Pb relative to sph-4. Some contact zones between sph-4 and sph-5 are enriched in Tl and In. All trace element maps are in counts per second (cps).

A second set of trace element maps was produced across a section containing sph-4 and a ferroan-dolomite vein containing sph-6 (Figure 9). The trace element maps reveal that sph-6 has relatively higher concentrations of Zn, Ge, Ga, Cd, In and Sn, and a lower concentration of Co, Ag, Sb and Tl relative to sph-4. This is in agreement with LA-ICP-MS spot analyses from sph-4 and sph-6, which indicate an enrichment in Zn, Ga, Ge and Sn and a depletion in Fe, Co, Ag, Sb and Tl in the chemically remobilised sphalerite. Sph-6 is zoned in the elements Cu, Ge, Ga, Cd, In and Sn. The zonation of Cu, Ge, Ga, In and Sn appear to correlate with each other, and anticorrelate with zones of high Cd (Figure 9).

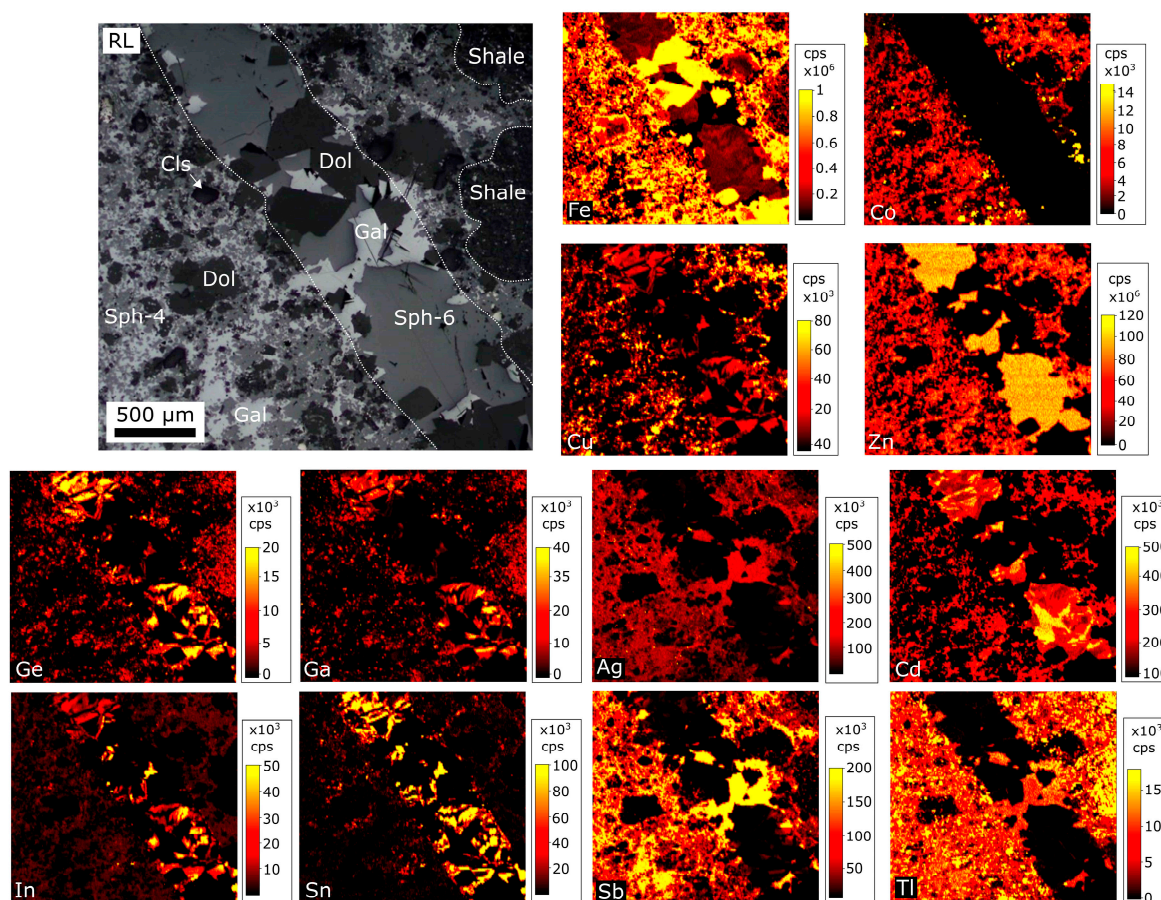


Figure 9. LA-ICP-MS trace element maps across a sample containing sph-4 and a ferroan-dolomite vein containing sph-6. The trace element maps indicate that sph-6 is enriched in Zn, Ge, Ga, Cd, In and Sn, and depleted in Fe, Co, Ag, Sb and Tl relative to sph-4. It is also seen that sph-6 is zoned in the elements Cu, Ge, Ga, Cd, In and Sn. All trace element maps are in counts per second (cps).

6. Discussion

6.1. Trace Element Substitution Mechanisms

A simple direct substitution for the bivalent elements Mn, Co and Cd with Fe is explained through the substitution mechanism (Mn^{2+} , Co^{2+} , $\text{Cd}^{2+} \leftrightarrow \text{Fe}^{2+}$; [7]). A positive correlation between Ag and Sb for all sphalerite varieties (Figure 10a; Supplementary Materials Table S3) is consistent with a dominant coupled substitution mechanism ($2\text{Zn}^{2+} \leftrightarrow \text{Ag}^+ + \text{Sb}^{3+}$) into sphalerite [13,39]. For sph-1 ($R = 0.52$), sph-2 ($R = 0.89$) and sph-4 ($R = 0.77$), Tl + Sn broadly correlate with the concentration of Ag + Sb (Figure 10b), indicating the presence of the substitution mechanisms $2\text{Zn}^{2+} \leftrightarrow (\text{Ag}^+ \text{ or } \text{Tl}^+) + \text{Sb}^{3+}$ and $3\text{Zn}^{2+} \leftrightarrow 2(\text{Ag}^+ \text{ or } \text{Tl}^+) + \text{Sn}^{4+}$. The substitution of trivalent and tetravalent elements Sb^{3+} , In^{3+} , Sn^{4+} , Ge^{4+} and Ga^{3+} with varying amounts of monovalent elements Ag^+ , Cu^+ and Tl^+ has been widely documented (Figure 10c; [7,40]), and is interpreted to represent the dominant substitution mechanism for the incorporation of these elements into the analysed sphalerite. A strong correlation between Ge and Cu (Figure 10d; Supplementary Materials Table S3) in sph-3 ($R = 0.99$) and sph-6 ($R = 0.70$) indicate the dominant mechanism for their substitution into sphalerite is $3\text{Zn}^{2+} \leftrightarrow \text{Ge}^{4+} + 2\text{Cu}^+$ [13], while no such correlation is shown by sph-1 ($R = -0.16$), sph-2 ($R = 0.10$) or sph-4 ($R = 0.06$).

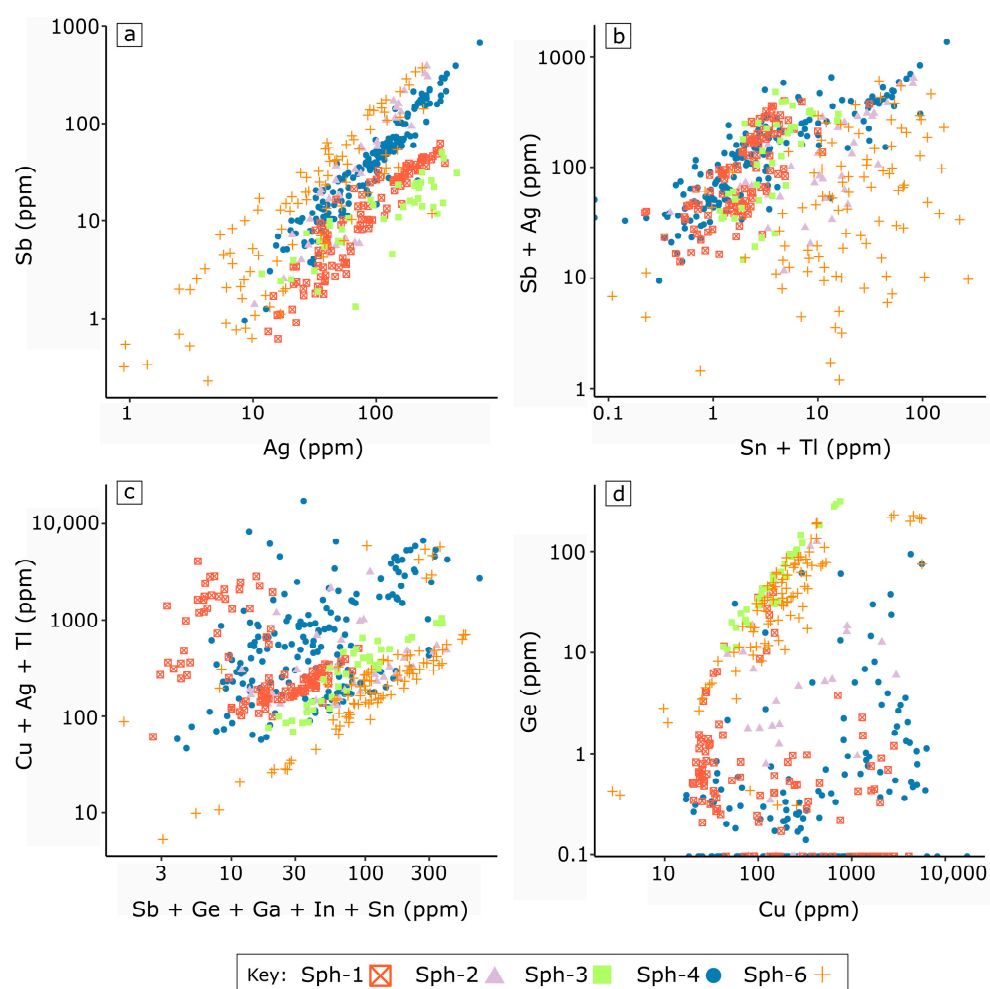


Figure 10. Binary scatter plots showing the correlation between trace elements in sphalerite and suggested substitution mechanisms. (a) Sb vs. Ag; (b) Sb + Ag vs. Sn + Tl; (c) Cu + Ag + Tl vs. Sb + Ge + Ga + In + Sn; (d) Ge vs. Cu.

6.2. Effects of Growth Conditions and Chemical Remobilisation on Sphalerite Geochemistry

6.2.1. Effect of Co-Crystallising Pyrite, Pyrrhotite and Galena

Sph-1 and sph-2 represent an early stratabound Zn mineralisation event. The timing and source of this stage of mineralisation is heavily debated and requires further investigation. Previous studies suggest that this stage of Zn-Pb mineralisation formed from an oxidised basinal brine coeval with the formation of host shale [14,41]. Studies from the nearby George Fisher Zn-Pb (Ag) deposit suggest that early Zn mineralisation post-dates the formation of the host shale, but pre-dates regional deformation [37,38]. This is challenged by work completed by Perkins and Bell [32] and Murphy [42], who favour the emplacement of early Zn-Pb mineralisation during D₄ deformation of the Isan Orogeny. Therefore, it is possible that this stage of mineralisation has undergone sub-greenschist facies metamorphism (~200 °C [30]) and subsequent deformation. Metamorphism can affect the distribution of trace elements in sphalerite, resulting in the crystallisation of discrete Ge-bearing minerals [10], and decrease the concentration of the elements Pb, Bi, Cu and Ag, which are often present in sphalerite as mineral inclusions containing these elements [43]. Detailed petrography and SEM work completed in this study did not detect any Ge-bearing minerals, and suggests that sph-1 does not exhibit any obvious textural features associated with deformation or recrystallisation, consistent with previous

work by Murphy [42]. Moreover, this study assumes that if regional-scale metamorphism is a factor, it would affect sph-1 and sph-2 equally.

Sph-2 is interpreted as the alteration product of sph-1. Although these two textural varieties occur near each other and are interpreted to have precipitated from the same fluid source, sph-1 co-crystallised alongside neighbouring pyrite, pyrrhotite and galena. As sph-2 is rarely associated with neighbouring sulphide phases, it allows us to examine the effect of co-existing sulphides (pyrrhotite, pyrite and galena) on the geochemistry of sphalerite.

Sph-2 contains significantly higher concentrations of Fe, Co, Ga, Ge, In, Sn, Sb and Tl relative to sph-1. Previous studies show that pyrite and pyrrhotite are the preferred host of Co in a typical sulphide assemblage [44,45]. Pyrite can also contain considerable concentrations of Tl, Sb and In [46–48]. Galena often contains trace amounts of Sn, Ge and Ga, and is the preferred host of Tl and Sb in a typical sulphide assemblage [5,49,50]. Fe is a core component of pyrrhotite ($\text{Fe}_{(0.8-1)}\text{S}$) and pyrite (FeS_2) (Figure 8), which, if co-crystallised with sphalerite, likely decrease the available Fe. Based on the preferred sulphide host of the elements listed above, it can be inferred that the co-crystallisation of neighbouring pyrite, pyrrhotite and galena resulted in the depletion of Fe, Co, In, Sb and Tl in sph-1 relative to sph-2, and possibly contributed to the relative depletion of Ga, Ge and Sn.

While the preferred host of Sn in the sulphide system is poorly constrained and shows no systematic pattern [5], sphalerite is the primary sulphide host of Ge and Ga [5]. The elements Ge, Ga and Sn are significantly enriched in chemically remobilised sphalerite types (Figures 7 and 9), reflecting highly soluble characteristics. A relatively high solubility would allow Ge, Ga and Sn to remain in the fluid during the precipitation of sph-2 alteration selvages, resulting in an enrichment of these elements in sph-2 compared to sph-1. Alternatively, both Ge and Ga are often enriched in carbonaceous sediments with high Al content [51–53], such as the Urquhart Shale. The infiltration of fluid through the shale could have leached additional Ge and Ga, which was incorporated into sph-2 during crystallisation.

6.2.2. Effect of Recrystallisation with Abundant Neighbouring Co-Crystallising Sulphides

At the nearby George Fisher Zn-Pb (Ag) deposit, breccia-hosted sphalerite is interpreted to have formed during early- D_4 deformation of the Isan Orogeny, representing in-situ deformed sph-1 veins [37]. However, this is disputed by Murphy [42], who found only minor evidence of sphalerite recrystallisation in the Zn-dominated breccias, favouring a D_4 timing for the formation of sph-4 mineralisation. Cu-rich mineralisation is interpreted to have been emplaced from late- D_2 to post- D_4 deformation of the Isan Orogeny [17], and represents the last stage of sulphide-rich mineralisation at the Hilton Zn-Pb (Ag) deposit.

Sph-5 is interpreted to represent the recrystallisation of sph-4 during the interaction with a subsequent Cu- and Pb-rich fluid. Therefore, sph-5 recrystallised with abundant neighbouring chalcopyrite, galena, pyrrhotite and pyrite (Figure 5c,d). A direct comparison between sph-4 and sph-5 allows us to study the effect that recrystallisation alongside abundant co-crystallising sulphides has on the geochemistry of sphalerite. Figure 8 shows that sph-5 is relatively depleted in Ga, Ge, Ag, In, Sn, Sb and Tl, and is relatively enriched in Zn, Cd and Pb relative to sph-4.

The highest concentrations of Sb is associated with the presence of galena, while Ag is concentrated in both chalcopyrite and galena (Figure 8). Therefore, it is suggested that during re-crystallisation, Ag and Sb were likely removed from sph-4, and preferentially incorporated into the co-crystallising chalcopyrite and galena.

In a typical sulphide assemblage, sphalerite is the preferred host of In, followed by chalcopyrite [5,46,50]. Therefore, it can be expected that upon the recrystallisation of sph-4 to form sph-5, a majority of liberated In would be preferentially re-incorporated into sph-5, with some of the In lost to co-crystallising chalcopyrite. This could explain the relative depletion of In within sph-5 relative to sph-4. However, Figure 8 indicates that sph-5 and co-crystallising chalcopyrite possess comparably low In concentrations. This could indicate that the late Cu- and Pb-rich fluid was

depleted in In, resulting in the In leached from sph-4 being redistributed over a large proportion of co-crystallising chalcopyrite and/or sph-5.

Sn does not have a predictable preferred sulphide host [5]. At Mount Isa, chalcopyrite is the preferred host of Sn, followed by galena then sphalerite [50]. Figure 8 indicates that sph-5 and co-crystallising chalcopyrite do not contain abundant Sn, and therefore it is unlikely that Sn was immediately redistributed into these neighbouring minerals. As discussed below (see Section 6.2.3.), Sn is concentrated in chemically remobilised sphalerite, indicating that it is readily expelled from the sphalerite lattice. This could suggest that Sn was transported away from the site of recrystallisation, and either incorporated into co-crystallising sulphides, such as galena and chalcopyrite elsewhere, or was lost to the late stage mineralising fluid.

Tl is also depleted in sph-5 relative to sph-4. In a typical sulphide assemblage, galena is the preferred sulphide host of Tl [5]. Figure 8 shows that sph-4 contains significantly more Tl than both sph-5 and associated co-crystallising galena. However, it is also shown that the galena contains a comparably higher concentration of Tl than sph-5 (Figure 8). Assuming the fluid associated with subsequent Cu- and Pb-rich mineralisation possessed a low concentration of Tl (as inferred by low Tl galena), and abundant neighbouring galena was present during the recrystallisation process (Figure 5c,d), it could be suggested that the Tl lost from the re-crystallisation of sph-4 was redistributed evenly among the abundant co-crystallising, low-Tl galena.

The heterogeneous distribution of Ge and Ga in sphalerite is shown in Figure 8. This suggests that high concentrations of these elements in the Hilton deposit are potentially associated with mineral inclusions. In a typical sulphide assemblage, Ga and Ge are preferentially concentrated into sphalerite, but can also be incorporated into chalcopyrite and galena [5,50]. In the Bergslagen ore province, Sweden, it has been shown that Ga is primarily hosted by Al-silicates and oxides [54]. Additionally, both Ga and Ge can be readily incorporated into feldspars through the direct substitution with Al and Si respectively [55]. Ge and Ga are highly mobile, and can be readily expelled from sphalerite during dissolution and re-precipitation reactions (see Section 6.2.3.) and metamorphism [10]. Therefore, the recrystallisation of sph-4 to form sph-5 would have resulted in the release of Ga and Ge from sph-4 and/or the mineral inclusions holding these elements into the fluid, where they were likely redistributed into clasts of Al-rich shale, feldspars and/or partitioned into co-crystallising sulphides such as chalcopyrite or galena.

Sphalerite is the primary host of Cd in a typical sulphide assemblage [5,56]. The concentration of Cd in sphalerite can be attributed to the temperature, Cd concentration or concentration of reduced sulphur in the ore-bearing fluid [56,57]. Cd-rich sphalerite typically precipitates from low-temperature fluids [57], or from fluids with low concentrations of reduced sulphur [56]. The Cu- and Pb-rich mineralisation stage that resulted in sph-5 is associated with higher-temperature conditions compared to sph-4 [14]. Therefore, the enrichment of Cd in sph-5 relative to sph-4 may be attributed to a higher concentration of Cd, or a lower concentration of reduced sulphur in the subsequent Cu- and Pb-rich fluid, promoting Cd enrichment [56].

Figure 8 shows that Zn is enriched in sph-5 relative to sph-4. This is consistent with the enrichment of Zn in chemically remobilised sphalerite relative to its parent material (see Section 6.2.3.). These results indicate that Zn can be readily leached and redistributed from sph-4 into sph-5 upon recrystallisation. As sphalerite is the primary Zn-mineral, any additional Zn associated with the subsequent Cu- and Pb-rich fluids would also be preferentially incorporated in sph-5, contributing to the relative enrichment.

Although the Pb trace element map is somewhat chaotic, Pb is enriched in sph-5 relative to sph-4 (Figure 8). As sph-5 is coeval with the emplacement of abundant galena, this likely reflects the increased concentration of Pb within the fluid, leading to an increase in the concentration of Pb-rich mineral inclusions in the coeval recrystallised sphalerite.

6.2.3. Effect of Chemical Remobilisation

Sph-3 and sph-6 are interpreted to have resulted from the chemical remobilisation of primary sph-1 and sph-4, respectively during initial fracturing and subsequent interstitial fluid flow. This allows us to examine the effect of chemical remobilisation on the geochemistry of sphalerite. Considering the relative timing of the previous styles of mineralisation, these veins are interpreted to have formed during late D₂, or syn-D₄, and post-D₄ deformation of the Isan Orogeny, respectively. Sphalerite in both sets of carbonate veins are interpreted to have formed from the same process associated with geochemically similar fluids, and are therefore compared together in this section.

Sph-3 and sph-6 are consistently enriched in Zn, Ga, Ge, Sn and Cd, and depleted in Co, Tl, Bi and Fe relative to the primary sph-1 and sph-4. Additionally, sph-6 is also depleted in Ag, Sb and Mn relative to sph-4.

Previous studies have shown that Ge will be readily expelled from the sphalerite lattice to form discrete Ge-S minerals upon metamorphism [10,58,59]. Additionally, Ga and Ge can be readily expelled during the recrystallisation of sphalerite (see Section 6.2.2.). It has been shown that Ge and Ga are preferentially concentrated in relatively low-temperature (~120 °C), moderate- to low-salinity fluids, leading to their enrichment in low-temperature ore deposits [7,8,11]. Therefore, it is interpreted that due to their relatively high mobility, Ge and Ga will be readily leached from the primary sphalerite and/or mineral inclusions hosting these elements during interstitial fluid flow, where they are incorporated into secondary sphalerite during crystallisation. Sn is geochemically similar Ge, with differences in the behaviour of Sn attributed to its 6.63% larger ionic size and its greater tendency for divalency [51]. The similar geochemical behaviour of Sn likely contributes to its ability to be easily expelled from the sphalerite lattice, where it is re-precipitated into secondary sphalerite, a process that is consistent with recrystallisation.

The formation of Cd-rich sphalerite is favoured by low-temperature fluids and/or low concentrations of reduced sulphur within the precipitating fluid [56,57]. It is suggested that significantly less mixing with the pyrite-rich host shale relative to all other mineralisation events, and the low-temperature formation of the ferroan-dolomite veins promoted Cd enrichment in the chemically remobilised sphalerite.

Previous studies have indicated a relationship between a higher precipitation temperature and an increased concentration of Co within sphalerite [60,61]. A temperature dependent relationship could explain the inability of Co to be mobilised from sphalerite during dissolution and re-precipitation mechanisms, resulting in the chemically remobilised sphalerite being significantly depleted in Co relative to the primary sphalerite.

Galena is the primary host of Tl, Sb, Ag and Bi in a typical sulphide assemblage [5]. The depletion in these elements in chemically remobilised sphalerite types relative to the primary sphalerite can be explained by their preferential partitioning into abundant neighbouring co-crystallising galena. This is consistent with Figure 9, which shows that the highest concentration of Tl, Sb and Ag in the late veins are associated with the presence of galena. Galena is more common in late ferroan-dolomite veins than in early ferroan-dolomite veins, explaining why sph-6 has a larger depletion in Ag, Bi, Sb and Tl relative to sph-6, compared to the depletion in these elements between sph-3 and sph-1.

The chemically remobilised sphalerite sph-3 and sph-6 are depleted in Fe and enriched in Zn relative to their parent material. Differences in the Fe and Zn content of chemically remobilised sphalerite can be attributed to the rate at which Fe and Zn can be leached from surrounding sphalerite, where Zn is leached more readily than Fe [62]. This interpretation is consistent with previous research by Wagner and Cook [63], who showed that the recrystallisation of sphalerite by a low Fe/Zn fluid produced a secondary sphalerite that was enriched in Zn and depleted in Fe relative to the primary sphalerite.

Alternatively, a substantial amount of Fe was likely partitioned into the co-crystallising ferroan-dolomite that makes up the dominant mineralogical component of these veins. Evidence for this is given by the high Fe values associated with ferroan-dolomite in Figure 9, which would decrease

the availability of Fe to the coeval chemically remobilised sphalerite. Moreover, competition with co-crystallising ferroan-dolomite would also explain the relative depletion of Mn in sph-6 compared to sph-4, which would also be preferentially incorporated into the ferroan-dolomite.

7. Conclusions

The identification of a complex paragenesis of six texturally distinct sphalerite types from the Hilton Zn-Pb deposit allows for evaluation of the effect that co-crystallising sulphides, recrystallisation and chemical remobilisation have on the trace element geochemistry of sphalerite.

- Sphalerite that has precipitated or recrystallised with neighbouring co-crystallising pyrite, pyrrhotite, galena and chalcopyrite is relatively depleted in the elements Fe, Co, In, Sn, Sb, Ag and Tl. This effect is due to the incorporation of these elements into the co-crystallising sulphide minerals.
- Sphalerite that is interpreted to have formed via chemical remobilisation is enriched in Zn, Ga, Ge and Sn, and depleted in Fe, Tl, Co, Bi, Ag, Sb and Mn relative to its parent material. The enrichment and depletion in trace elements from chemically remobilised sphalerite reflect their relative mobility, which allows them to be leached from the primary sphalerite into the secondary sphalerite. The relative depletion of Bi, Tl, Ag, and Sb in chemically remobilised sphalerite is associated with abundant co-crystallising galena, while the depletion in Fe and Mn may be attributed to co-crystallising ferroan-dolomite.

Overall, results from this study indicate that co-crystallising sulphides and/or chemical remobilisation greatly affect the trace element composition of sphalerite, in particular concentrating or depleting high-demand critical metals including Ge, Ga and In. We suggest that these factors are important to understanding the trace element geochemistry of sphalerite on a variety of scales and have potential implications for a range of Zn-Pb deposits worldwide.

Supplementary Materials: The following are available online at <http://www.mdpi.com/2075-163X/10/9/797/s1>, Table S1: EPMA vs LA-ICP-MS, Table S2: Sphalerite Geochemistry, Table S3: Element Correlation Matrix.

Author Contributions: B.C. conceived this contribution, performed analytical work, reduced the data and wrote the article. R.L. and W.H. assisted in writing, draft preparation and editing. Funding was acquired by R.L., who also assisted in study design. All authors have read and agreed to the published version of the manuscript.

Funding: This study was funded by Mount Isa Mines—a Glencore Company and forms part of the Mount Isa Research for Geology and Exploration (MIRGE) project.

Acknowledgments: I would like to thank the many geologists at the George Fisher Mine and the Mount Isa Exploration team for their warm hospitality during fieldwork and assistance during sampling. I would also like to thank Sarah Gilbert, Ben Wade and Aoife McFadden from Adelaide Microscopy for assistance with analytical procedures. Furthermore, I would also like to thank Karin Barovich, who greatly assisted in writing and drafting this manuscript. B.C. is supported by the Australian Government Research Training Program. MinEx CRC is thanked for supporting W.H. for involving this research.

Conflicts of Interest: The authors declare no conflict of interest. The funders had no role in the design of the study; in the collection, analyses, or interpretation of data; in the writing of the manuscript, or in the decision to publish the results.

References

1. Zhang, S.; Ding, Y.; Liu, B.; Chang, C. Supply and demand of some critical metals and present status of their recycling in WEEE. *Waste Manag.* **2017**, *65*, 113–127. [[CrossRef](#)] [[PubMed](#)]
2. Watari, T.; Nansai, K.; Nakajima, K. Review of critical metal dynamics to 2050 for 48 elements. *Resour. Conserv. Recycl.* **2020**, *155*, 104669. [[CrossRef](#)]
3. Cook, N.J.; Ciobanu, C.L. Mineral hosts for critical metals in hydrothermal ores. In Proceedings of the Mineral Resources in a Sustainable World, 13th SGA Biennial Meeting, Nancy, France, 24–27 August 2015; pp. 24–27.
4. Sinclair, W.D. Electronic metals (In, Ge and Ga): Present and future resources. *Acta Geol. Sin. Ed.* **2014**, *88*, 463–465. [[CrossRef](#)]

5. George, L.L.; Cook, N.J.; Ciobanu, C.L. Partitioning of trace elements in co-crystallized sphalerite–galena–chalcopyrite hydrothermal ores. *Ore Geol. Rev.* **2016**, *77*, 97–116. [[CrossRef](#)]
6. Bauer, M.E.; Seifert, T.; Burisch, M.; Krause, J.; Richter, N.; Gutzmer, J. Indium-bearing sulfides from the Hämmerlein skarn deposit, Erzgebirge, Germany: Evidence for late-stage diffusion of indium into sphalerite. *Miner. Depos.* **2019**, *54*, 175–192. [[CrossRef](#)]
7. Cook, N.J.; Ciobanu, C.L.; Pring, A.; Skinner, W.; Shimizu, M.; Danyushevsky, L.; Saini-Eidukat, B.; Melcher, F. Trace and minor elements in sphalerite: A LA-ICPMS study. *Geochim. Cosmochim. Acta* **2009**, *73*, 4761–4791. [[CrossRef](#)]
8. Frenzel, M.; Hirsch, T.; Gutzmer, J. Gallium, germanium, indium, and other trace and minor elements in sphalerite as a function of deposit type—A meta-analysis. *Ore Geol. Rev.* **2016**, *76*, 52–78. [[CrossRef](#)]
9. Ye, L.; Cook, N.J.; Ciobanu, C.L.; Yuping, L.; Qian, Z.; Tiegeng, L.; Wei, G.; Yulong, Y.; Danyushevskiy, L. Trace and minor elements in sphalerite from base metal deposits in South China: A LA-ICPMS study. *Ore Geol. Rev.* **2011**, *39*, 188–217. [[CrossRef](#)]
10. Cugerone, A.; Cenki-Tok, B.; Oliot, E.; Muñoz, M.; Barou, F.; Motto-Ros, V.; Le Goff, E. Redistribution of germanium during dynamic recrystallization of sphalerite. *Geology* **2019**, *48*, 236–241. [[CrossRef](#)]
11. Bauer, M.E.; Burisch, M.; Ostendorf, J.; Krause, J.; Frenzel, M.; Seifert, T.; Gutzmer, J. Trace element geochemistry of sphalerite in contrasting hydrothermal fluid systems of the Freiberg district, Germany: Insights from LA-ICP-MS analysis, near-infrared light microthermometry of sphalerite-hosted fluid inclusions, and sulfur isotope geochemi. *Miner. Depos.* **2019**, *54*, 237–262. [[CrossRef](#)]
12. Henjes-Kunst, E.; Raith, J.G.; Boyce, A.J. Micro-scale sulfur isotope and chemical variations in sphalerite from the Bleiberg Pb-Zn deposit, Eastern Alps, Austria. *Ore Geol. Rev.* **2017**, *90*, 52–62. [[CrossRef](#)]
13. Wei, C.; Ye, L.; Hu, Y.; Danyushevskiy, L.; Li, Z.; Huang, Z. Distribution and occurrence of Ge and related trace elements in sphalerite from the Lehong carbonate-hosted Zn-Pb deposit, northeastern Yunnan, China: Insights from SEM and LA-ICP-MS studies. *Ore Geol. Rev.* **2019**, *115*, 103175. [[CrossRef](#)]
14. Valenta, R. Deformation, fluid flow and mineralization in the Hilton area, Mt Isa, Australia. Ph.D. Thesis, Monash University, Melbourne, Australia, June 1988.
15. Wilson, A. Metal Distribution in the Hilton Mine, Mount Isa and its Genetic Implications. Honours Thesis, Monash University, Melbourne, Australia, 1992.
16. Valenta, R. Deformation of host rocks and stratiform mineralization in the Hilton Mine area, Mt Isa. *Aust. J. Earth Sci.* **1994**, *41*, 429–443. [[CrossRef](#)]
17. Valenta, R. Syntectonic discordant copper mineralization in the Hilton Mine, Mount Isa. *Econ. Geol.* **1994**, *89*, 1031–1052. [[CrossRef](#)]
18. Southgate, P.N. Carpentaria-Mt Isa Zinc Belt: Basement framework, chronostratigraphy and geodynamic evolution of Proterozoic successions. *Aust. J. Earth Sci.* **2000**, *47*, 337–340. [[CrossRef](#)]
19. Page, R.W.; Jackson, M.J.; Krassay, A.A. Constraining sequence stratigraphy in north Australian basins: SHRIMP U–Pb zircon geochronology between Mt Isa and McArthur River. *Aust. J. Earth Sci.* **2000**, *47*, 431–459. [[CrossRef](#)]
20. Southgate, P.N.; Neumann, N.L.; Gibson, G.M. Depositional systems in the Mt Isa Inlier from 1800 Ma to 1640 Ma: Implications for Zn–Pb–Ag mineralisation. *Aust. J. Earth Sci.* **2013**, *60*, 157–173. [[CrossRef](#)]
21. Domagala, J.; Southgate, P.N.; McConachie, B.A.; Pidgeon, B.A. Evolution of the Palaeoproterozoic Prize, Gun and lower Loretta Supersequences of the Surprise Creek Formation and Mt Isa Group. *Aust. J. Earth Sci.* **2000**, *47*, 485–507. [[CrossRef](#)]
22. Scott, D.L.; Rawlings, D.J.; Page, R.W.; Tarlowski, C.Z.; Idnurm, M.; Jackson, M.J.; Southgate, P.N. Basement framework and geodynamic evolution of the Palaeoproterozoic superbasins of north-central Australia: An integrated review of geochemical, geochronological and geophysical data. *Aust. J. Earth Sci.* **2000**, *47*, 341–380. [[CrossRef](#)]
23. Betts, P.G.; Giles, D.; Mark, G.; Lister, G.S.; Goleby, B.R.; Aillères, L. Synthesis of the Proterozoic evolution of the Mt Isa Inlier. *Aust. J. Earth Sci.* **2006**, *53*, 187–211. [[CrossRef](#)]
24. Neumann, N.L.; Southgate, P.N.; Gibson, G.M.; McIntyre, A. New SHRIMP geochronology for the Western Fold Belt of the Mt Isa Inlier: Developing a 1800–1650 Ma event framework. *Aust. J. Earth Sci.* **2006**, *53*, 1023–1039. [[CrossRef](#)]
25. Page, R.W.; Bell, T.H. Isotopic and structural responses of granite to successive deformation and metamorphism. *J. Geol.* **1986**, *94*, 365–379. [[CrossRef](#)]

26. Winsor, C.N. Intermittent folding and faulting in the Lake Moondarra area, Mount Isa, Queensland. *Aust. J. Earth Sci.* **1986**, *33*, 27–42. [[CrossRef](#)]
27. Connors, K.A.; Page, R.W. Relationships between magmatism, metamorphism and deformation in the western Mount Isa Inlier, Australia. *Precambrian Res.* **1995**, *71*, 131–153. [[CrossRef](#)]
28. Duncan, R.J.; Wilde, A.R.; Bassano, K.; Maas, R. Geochronological constraints on tourmaline formation in the Western Fold Belt of the Mount Isa Inlier, Australia: Evidence for large-scale metamorphism at 1.57 Ga? *Precambrian Res.* **2006**, *146*, 120–137. [[CrossRef](#)]
29. Hand, M.; Rubatto, D. The scale of the thermal problem in the Mt Isa Inlier. In *Geological Society of Australia Abstracts*; Geological Society of Australia: Hornsby, Australia, 2002; Volume 67, p. 173.
30. Chapman, L.H. Geology and Genesis of the George Fisher Zn-Pb-Ag deposit Mount Isa, Australia. Ph.D. Thesis, James Cook University, Townsville, Australia, 1999.
31. Bell, T.H.; Hickey, K.A. Multiple deformations with successive subvertical and subhorizontal axial planes in the Mount Isa region; their impact on geometric development and significance for mineralization and exploration. *Econ. Geol.* **1998**, *93*, 1369–1389. [[CrossRef](#)]
32. Perkins, W.G.; Bell, T.H. Stratiform replacement lead-zinc deposits; a comparison between Mount Isa, Hilton, and McArthur River. *Econ. Geol.* **1998**, *93*, 1190–1212. [[CrossRef](#)]
33. Danyushevsky, L.; Robinson, P.; Gilbert, S.; Norman, M.; Large, R.; McGoldrick, P.; Shelley, M. Routine quantitative multi-element analysis of sulphide minerals by laser ablation ICP-MS: Standard development and consideration of matrix effects. *Geochemistry Explor. Environ. Anal.* **2011**, *11*, 51–60. [[CrossRef](#)]
34. Norris, A.; Danyushevsky, L. *Towards Estimating the Complete Uncertainty Budget of Quantified Results Measured by LA-ICPMS*; Goldschmidt: Boston, MA, USA, 2018.
35. Paton, C.; Hellstrom, J.; Paul, B.; Woodhead, J.; Hergt, J. Iolite: Freeware for the visualisation and processing of mass spectrometric data. *J. Anal. At. Spectrom.* **2011**, *26*, 2508–2518. [[CrossRef](#)]
36. Woodhead, J.D.; Hellstrom, J.; Hergt, J.M.; Greig, A.; Maas, R. Isotopic and elemental imaging of geological materials by laser ablation inductively coupled plasma-mass spectrometry. *Geostand. Geoanalytical Res.* **2007**, *31*, 331–343. [[CrossRef](#)]
37. Chapman, L.H. Geology and mineralization styles of the George Fisher Zn-Pb-Ag deposit, Mount Isa, Australia. *Econ. Geol.* **2004**, *99*, 233–255. [[CrossRef](#)]
38. Rieger, P.; Magnall, J.M.; Gleeson, S.A.; Lilly, R.; Rocholl, A.; Kusebauch, C. Sulfur Isotope Constraints on the Conditions of Pyrite Formation in the Paleoproterozoic Urquhart Shale Formation and George Fisher Zn-Pb-Ag Deposit, Northern Australia. *Econ. Geol.* **2020**. [[CrossRef](#)]
39. Yuan, B.; Zhang, C.; Yu, H.; Yang, Y.; Zhao, Y.; Zhu, C.; Ding, Q.; Zhou, Y.; Yang, J.; Xu, Y. Element enrichment characteristics: Insights from element geochemistry of sphalerite in Daliangzi Pb-Zn deposit, Sichuan, Southwest China. *J. Geochem. Explor.* **2018**, *186*, 187–201. [[CrossRef](#)]
40. Belissont, R.; Boiron, M.-C.; Luais, B.; Cathelineau, M. LA-ICP-MS analyses of minor and trace elements and bulk Ge isotopes in zoned Ge-rich sphalerites from the Noailhac-Saint-Salvy deposit (France): Insights into incorporation mechanisms and ore deposition processes. *Geochim. Cosmochim. Acta* **2014**, *126*, 518–540. [[CrossRef](#)]
41. Cooke, D.R.; Bull, S.W.; Large, R.R.; McGoldrick, P.J. The importance of oxidized brines for the formation of Australian Proterozoic stratiform sediment-hosted Pb-Zn (Sedex) deposits. *Econ. Geol.* **2000**, *95*, 1–18. [[CrossRef](#)]
42. Murphy, T.E. Structural and Stratigraphic Controls on Mineralization at the George Fisher Zn-Pb-Ag Deposit, Northwest Queensland, Australia. Ph.D. Thesis, James Cook University, Townsville, Australia, 2004.
43. Lockington, J.A.; Cook, N.J.; Ciobanu, C.L. Trace and minor elements in sphalerite from metamorphosed sulphide deposits. *Mineral. Petrol.* **2014**, *108*, 873–890. [[CrossRef](#)]
44. Campbell, F.A.; Ethier, V.G. Nickel and cobalt in pyrrhotite and pyrite from the Faro and Sullivan orebodies. *Can. Mineral.* **1984**, *22*, 503–506.
45. Witt, W.K.; Hagemann, S.G.; Roberts, M.; Davies, A. Cobalt enrichment at the Juomasuo and Hangaslampi polymetallic deposits, Kuusamo Schist Belt, Finland: A role for an orogenic gold fluid? *Miner. Depos.* **2019**, *55*, 1–8. [[CrossRef](#)]
46. Frenzel, M.; Bachmann, K.; Carvalho, J.R.S.; Relvas, J.M.R.S.; Pacheco, N.; Gutzmer, J. The geometallurgical assessment of by-products—Geochemical proxies for the complex mineralogical development of indium at Neves-Corvo, Portugal. *Miner. Depos.* **2018**, *54*, 1–24. [[CrossRef](#)]

47. George, L.L.; Biagioni, C.; Lepore, G.O.; Lacalamita, M.; Agrosi, G.; Capitani, G.C.; Bonaccorsi, E.; d’Acapito, F. The speciation of thallium in (Tl, Sb, As)-rich pyrite. *Ore Geol. Rev.* **2019**, *107*, 364–380. [[CrossRef](#)]
48. Grant, H.L.J.; Hannington, M.D.; Petersen, S.; Frische, M.; Fuchs, S.H. Constraints on the behavior of trace elements in the actively-forming TAG deposit, Mid-Atlantic Ridge, based on LA-ICP-MS analyses of pyrite. *Chem. Geol.* **2018**, *498*, 45–71. [[CrossRef](#)]
49. George, L.; Cook, N.J.; Ciobanu, C.L.; Wade, B.P. Trace and minor elements in galena: A reconnaissance LA-ICP-MS study. *Am. Mineral.* **2015**, *100*, 548–569. [[CrossRef](#)]
50. Cave, B.; Lilly, R.; Barovich, K. Textural and geochemical analysis of chalcopyrite, galena and sphalerite across the Mount Isa Cu to Pb-Zn transition: Implications for a zoned Cu-Pb-Zn system. *Ore Geol. Rev.* **2020**, *124*, 103647. [[CrossRef](#)]
51. Höll, R.; Kling, M.; Schroll, E. Metallogenesis of germanium—A review. *Ore Geol. Rev.* **2007**, *30*, 145–180. [[CrossRef](#)]
52. Burton, J.D.; Culkin, F.; Riley, J.P. The abundances of gallium and germanium in terrestrial materials. *Geochim. Cosmochim. Acta* **1959**, *16*, 151–180. [[CrossRef](#)]
53. Bernstein, L.R. Germanium geochemistry and mineralogy. *Geochim. Cosmochim. Acta* **1985**, *49*, 2409–2422. [[CrossRef](#)]
54. Jonsson, E.; Högdahl, K. On the occurrence of gallium and germanium in the Bergslagen ore province, Sweden. *GFF* **2019**, *141*, 48–53. [[CrossRef](#)]
55. Goldsmith, J.R. Gallium and germanium substitutions in synthetic feldspars. *J. Geol.* **1950**, *58*, 518–536. [[CrossRef](#)]
56. Schwartz, M.O. Cadmium in zinc deposits: Economic geology of a polluting element. *Int. Geol. Rev.* **2000**, *42*, 445–469. [[CrossRef](#)]
57. Wen, H.; Zhu, C.; Zhang, Y.; Cloquet, C.; Fan, H.; Fu, S. Zn/Cd ratios and cadmium isotope evidence for the classification of lead-zinc deposits. *Sci. Rep.* **2016**, *6*, 1–8. [[CrossRef](#)]
58. Cugerone, A.; Cenki-Tok, B.; Chauvet, A.; Le Goff, E.; Bailly, L.; Alard, O.; Allard, M. Relationships between the occurrence of accessory Ge-minerals and sphalerite in Variscan Pb-Zn deposits of the Bossost anticlinorium, French Pyrenean Axial Zone: Chemistry, microstructures and ore-deposit setting. *Ore Geol. Rev.* **2018**, *95*, 1–19. [[CrossRef](#)]
59. Cugerone, A.; Cenki-Tok, B.; Muñoz, M.; Kouzmanov, K.; Olliot, E.; Motto-Ros, V.; Le Goff, E. Behavior of critical metals in metamorphosed Pb-Zn ore deposits: Example from the Pyrenean Axial Zone. *Miner. Depos.* **2020**, 1–21. [[CrossRef](#)]
60. Lee, J.H.; Yoo, B.C.; Yang, Y.-S.; Lee, T.H.; Seo, J.H. Sphalerite Geochemistry of the Zn-Pb Orebodies in the Taebaeksan Metallogenic Province, Korea. *Ore Geol. Rev.* **2019**, *107*, 1046–1067. [[CrossRef](#)]
61. Wang, Y.; Han, X.; Petersen, S.; Frische, M.; Qiu, Z.; Cai, Y.; Zhou, P. Trace Metal Distribution in Sulfide Minerals from Ultramafic-Hosted Hydrothermal Systems: Examples from the Kairei Vent Field, Central Indian Ridge. *Minerals* **2018**, *8*, 526. [[CrossRef](#)]
62. Stanton, M.R.; Gemery-Hill, P.A.; Shanks, W.C., III; Taylor, C.D. Rates of zinc and trace metal release from dissolving sphalerite at pH 2.0–4.0. *Appl. Geochem.* **2008**, *23*, 136–147. [[CrossRef](#)]
63. Wagner, T.; Cook, N.J. Sphalerite remobilization during multistage hydrothermal mineralization events—Examples from siderite-Pb-Zn-Cu-Sb veins, Rheinisches Schiefergebirge, Germany. *Mineral. Petrol.* **1998**, *63*, 223–241. [[CrossRef](#)]

